JOURNAL OF AIRCRAFT
Vol. 47, No. 3, May–June 2010

Unsteady Lift Generation on Rotating Wings at Low Reynolds Numbers

A. R. Jones* and H. Babinsky†
University of Cambridge, Cambridge, England CB2 1PZ, United Kingdom

DOI: 10.2514/1.46649

The rotating wing experiment is a fully three-dimensional simplification of the flapping-wing motion observed in nature. The spanwise velocity gradient and the wing starting and stopping acceleration that exist on an insectlike flapping wing are generated by the rotational motion of a finite-span wing. The flow development around a rotating wing at $Re = 60,000$ has been studied using high-speed particle image velocimetry to capture the unsteady velocity field. Lift and drag forces have been measured for several different sets of wing kinematics and angles of attack. The lift curve shape was similar in all cases. A transient high lift peak, approximately 1.5 times the quasi-steady value, occurred in the first chord length of travel, and it was caused by the formation of a strong attached leading-edge vortex. This vortex then separated from the leading edge, resulting in a sharp drop in lift. As weaker leading-edge vortices continued to form and shed, lift values recovered to an intermediate value. The circulation of the leading-edge vortex has been measured and agrees well with the force data. Wing kinematics had only a small effect on the aerodynamic forces produced by the waving wing. In the early stages of the wing stroke, the velocity profiles with low accelerations affected the timing and the magnitude of the lift peak, but at higher accelerations, the velocity profile was insignificant.

Nomenclature

C_D	=	drag coefficient
C_L	=	lift coefficient
c	=	wing chord, m
k	=	reduced frequency, $\omega b/U$
Re	=	Reynolds number, $\rho U c/\mu$
U	=	local freestream, m/s
x	=	distance traveled, m
α	=	angle of attack
Γ	=	circulation, m^3/s
λ	=	scalar measure of fluid rotation
μ	=	dynamic viscosity, $kg/m \cdot s$
ρ	=	density of water, kg/m^2
ω	=	angular velocity, rad/s

I. Introduction

CURRENT micro-air-vehicle (MAV) designs are inspired by natural fliers, but none approach the efficiency or functionality demonstrated by birds and insects. Bird and insect flight is affected by a steep decline in airfoil performance between the Reynolds numbers of 10^4 and 10^5, marking the boundary between steady and unsteady lift-generating mechanisms observed in nature [1]. Flight in this Reynolds number regime is primarily flapping-wing flight, and it is generally thought that some form of unsteady aerodynamic phenomena are necessary to achieve the necessary lift coefficients. It is in this regime that MAVs must generate sufficient lift and perform maneuvers in both calm and gusty conditions. Although many unsteady flow effects have been identified so far, the relative importance of these phenomena and the significance of three-dimensionality are not well understood.

Received 10 August 2009; revision received 7 January 2010; accepted for publication 9 January 2010.

*Ph.D. Research Student, Aerodynamics Laboratory, Department of Engineering, Trumpington Street. AIAA Student Member.

†Reader in Aerodynamics, Aerodynamics Laboratory, Department of Engineering, Trumpington Street. AIAA Senior Member.

Figure 1 is an overview of the maximum lift coefficients reported in the literature across a range of Reynolds numbers. The shaded data (smooth airfoils, airfoils with turbulators, and insect wings) represent experiments in steady flow. The remaining data represent unsteady or three-dimensional experiments: hovering insects refers to data collected using tethered insects and revolving wings refers to propellerlike experiments [2,3]. At $Re > 10^5$, birds use many common flow control methods (trips, injection, etc.) to influence boundary-layer transition [4–7]. In this regime, separated flow quickly becomes turbulent and often reattaches, generating lift in steady flow. At very low Reynolds numbers ($Re < 10^4$), the flow about the flapping wings remains laminar and is highly separated.

As lift in steady flow is limited in the Reynolds number range of interest for MAV flight, it is necessary to turn toward unsteady aerodynamics in search of a robust way to produce lift. One natural source of inspiration is insect flight. The insect wing stroke consists of two translational half-strokes, which make up 80–90% of the stroke, and two rotational motions. The stroke amplitude can vary from 66 to 180 deg, corresponding to two to five chord lengths. Wing motion is nearly harmonic with higher accelerations at the beginning and the ending of the stroke, and a constant velocity is near the middle of the stroke [8,9].

Experiments on insectlike flapping wings present two immediate difficulties: creating a clean flow at very low Reynolds numbers and observing and measuring the complicated flow patterns that arise from the full set of insect-wing-flapping kinematics. Previous studies have relied on mechanical wing flappers designed to mimic these kinematics over a wide range of Reynolds numbers [10–16]. Each of these studies has identified a leading-edge vortex (LEV) responsible for a significant portion of the lift generated. The strength and stability of this LEV appears to depend on a number of variables, but it is difficult to isolate the effects of the Reynolds number, the wing shape, the translation, the rotation, and the angle of attack in such a complicated flowfield.

Much simpler flows can be obtained from an impulsively started wing, inspired by the start of the translational phase of an insect wing stroke [17–20]. Although useful for fundamental studies, this model oversimplifies the wing kinematics. Pure translation does not preserve the velocity gradient from root to tip, thus potentially eliminating the spanwise flow that is likely to effect the stability of the LEV. Another approach is to investigate airfoils undergoing a pitch and plunge motion [21–23]. Although useful for fundamental studies of flapping lift and thrust, this approach neglects the three-dimensionality of the flow.

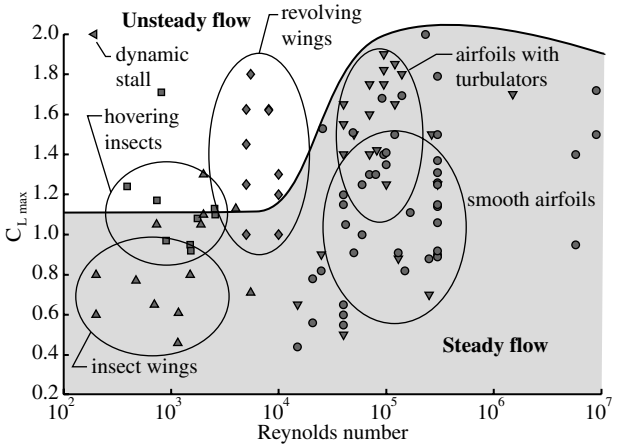

Fig. 1 Maximum lift coefficient versus Reynolds number.

Altshuler et al. [3], Usherwood and Ellington [24,25], and Nolan [26] performed experiments on a quasi-steady setup in which the wing rotated like a propeller. This model preserves the three-dimensional flow as a velocity gradient, but it neglects the starting and stopping that occur at the beginning and the end of the translational phase of the insect wing stroke. As an insect wing stroke is only two to five chord lengths [8,9,27], these accelerations are expected to have a significant effect on the flowfield. Nevertheless, propeller experiments have greatly helped to understand the attached LEV, first observed on mechanical wing flappers, and demonstrated that this vortex can generate sufficient lift. It remains unclear how quickly the flow develops and to what extent lessons learned from quasi-steady propeller experiments can be applied to truly unsteady flapping.

Recently, more work has been done on propellerlike revolving wings. Computational fluid dynamics (CFD) simulations have captured the leading-edge separation that causes the formation of a LEV. This vortex remains attached to the leading edge for the first two chord lengths of travel before separating. Force predictions suggest a period of low lift for the first 50 deg of rotation. After this point, the lift rises and levels off after about 90 deg of sweep. Experiments show that the lift does not actually level off until several revolutions have passed, but it does plateau near 90 deg. This discrepancy is attributed to the wake capture, which is not modeled in the computations [20].

Others have shown that the highly unsteady effects at the beginning and the end of the flapping cycle can produce significant additional lift, but it is unclear what the relative importance of these effects are [14]. A further uncertainty arises from the fact that all of the previously mentioned experiments are concentrated at very low Reynolds numbers, and the existence of a stable LEV at higher MAV-like Reynolds numbers is still uncertain.

The aim of the research presented here is to understand unsteady lift generation at Reynolds numbers typical for MAVs ($10,000 \leq Re \leq 60,000$). In particular, the significance of three-dimensional effects is to be determined. Because the presence of a stable LEV is thought to be crucial for the production of high lift coefficients at low Reynolds numbers, the question addressed here is whether such an LEV develops at Reynolds numbers above 10,000 and to what extent three-dimensionality is necessary to sustain it. There are two aspects to three-dimensionality, first in terms of the wing planform (finite span) and second in the motion (rotating versus sliding), and both are thought to affect the flow development. Finally, the time scale of unsteady effects is addressed.

The waving-wing experiment is designed to produce a simple yet fully three-dimensional and unsteady flowfield. A sliding wing, as studied by Beckwith and Babinsky, preserves the geometric effects of three-dimensionality but with uniform flow across the wing [19]. In contrast, the waving wing experiences a spanwise velocity gradient in the same manner as the propeller experiments, but in this setup, the acceleration at the beginning and the end of the wing stroke is preserved as well. This model of the translational phase of an insect wing stroke allows for the identification of lift-generating flow structures and the quantification of the relative importance of steady and unsteady effects, and it provides data that can be used to validate unsteady three-dimensional CFD results.

II. Experimental Methods

All experiments have been conducted by towing or rotating a wing model through a tank filled with still water. By using water as the working medium, it is possible to achieve the required Reynolds numbers with relatively slow motions, allowing for very high temporal resolution, while at the same time providing an optimal environment for force measurements and optical flow diagnostics. Allowing sufficient time between experiments, the residual free-stream turbulence is below the measurement uncertainty.

A. Impulsively Started Wing

Two types of experiments have been performed, both using similar wing geometry but different kinematics. The first is an impulsively started flat-plate wing moving in a sliding motion, similar to a fixed wing. Details of these experiments and a full discussion of the results are provided by Beckwith and Babinsky [19]. The desired Reynolds number of 60,000 was achieved with a towing speed of 0.48 $\mathrm{m\,s^{-1}}$. The wing underwent a constant acceleration from rest to full speed over a streamwise distance of 0.072 m, equivalent to 0.60 chords.

B. Waving Wing Experiment

The waving-wing mechanism was designed to mimic the translational phases of an insect wing stroke, extending the propeller experiments to include wing starting and stopping. The wing is started from rest and swept through a wing-stroke angle θ up to 90 deg, with or without a freestream generated by translating the mechanism via a towing tank carriage. The wing's angular velocity can be programmed to any profile.

The Cambridge University Engineering Department's towing tank is 7 m long and has a 1×1 m cross section with a central 2-m-long Perspex test section. A sketch and a photo of the waving arm mechanism are shown in Fig. 2. Here, the entire setup is shown suspended from the tow tank carriage on four vertical struts. The Perspex sides and the water volume of the tank are shown to provide a sense of scale. The water depth is 0.8 m.

The mechanism is mounted on a stainless steel plate suspended just below the water surface. The waving motion is controlled by a servomotor and gearbox programmable through LabView, and a slotted optical switch is mounted near one end of the axle to confirm wing position. A force balance can be mounted on the wing to provide unsteady lift and drag force measurements. The distance from the wing root (defined as the bottom of the skim plate when the wing is vertical) to the axis of rotation is 10% of the span, similar to previous propeller experiments [26]. The angle of attack is selectable from 0 to 45 deg in 5 deg increments. The wing is a 2.5%-thick carbon-fiber flat plate with rounded edges, a chord of 0.125 m, and an aspect ratio of 4, as measured from the free surface to the wing tip. A 90 deg wing stroke is equivalent to 5.37 chords of travel at a three-quarter span. At a 15 deg angle of attack, blockage of the towing tank is 2%.

To ensure the lowest possible freestream turbulence for each repetition of the experiment, a particle image velocimetry (PIV) system was used to determine the turbulence intensity. The tank was allowed to settle overnight, then a disturbance was introduced: the tank was stirred (as when mixing in seed particles) for PIV, or the waving-wing mechanism was moved as for a wing stroke. The velocity field was measured at set times past the disturbance. The turbulence intensity was calculated up to 2 h past the disturbance and again overnight, never dropping below about 0.4%. This suggests that the actual turbulence is likely to be lower than that value, but measurements are limited by the capabilities of the PIV system. Based on these results, the tank was allowed to settle for 30 min after mixing in the PIV particles and 10 min between wing strokes.

The wing stroke was programmed using three different velocity profiles: linear, sinusoidal, and exponential in time, as shown in Figs. 3 and 4. The wing was accelerated, such that it reached its

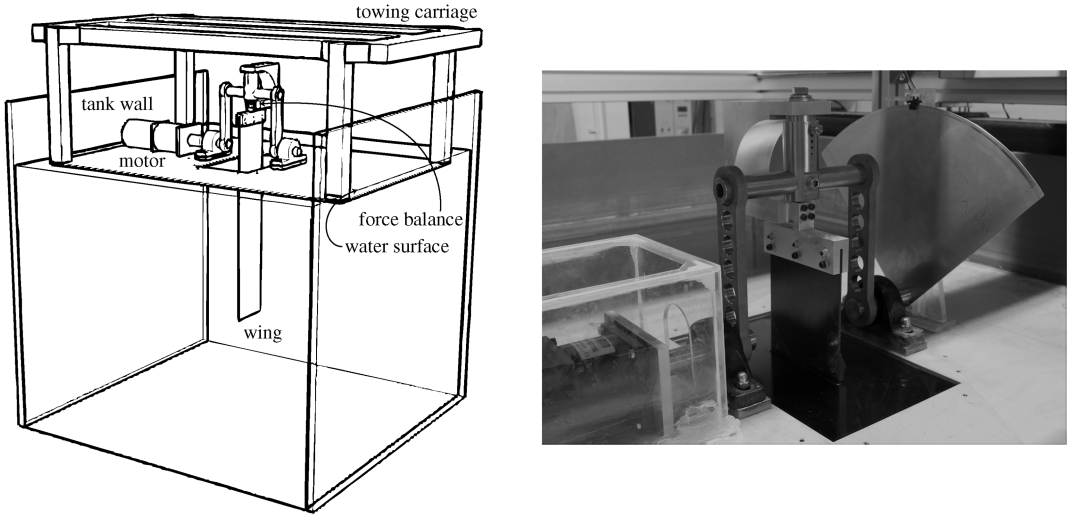

Fig. 2 The waving-wing mechanism.

maximum velocity after 0.10 (exponential only), 0.25, or 0.60 chord lengths of travel for each profile. Velocity profiles were symmetric, such that the wing decelerated in the same way before reaching a maximum stroke angle of 90 deg. The maximum velocity was chosen as one which gave a local wing Reynolds number of 60,000 at a three-quarter span.

C. Force Measurements

A water-resistant force balance has been designed and fabricated. The force balance is capable of measuring two force components to 10 N with a resolution of at least 0.01 N. When paired with a Fylde FE-379-TA transducer amplifier and a National Instruments USB-6221 multifunction data acquisition module, unsteady lift and drag forces can be measured at frequencies up to 250 kHz.

Two-component force balance measurements were taken in both the air and water for the wing waving through 90 deg (5.37 chord lengths of travel at a three-quarter span). Data was sampled at 7 kHz, with and without a 30 Hz low-pass filter. Wing lift and drag coefficients were obtained by subtracting the inertial forces measured in the air from the forces measured in the water and by normalizing by the local wing velocity, such that $C_L = 6L/[\rho\omega^2 c(r_t^3 - r_r^3)]$, where r_t and r_r are the distances from the axis of rotation to the wing tip and the wing root. Force data were averaged over five runs.

Figure 5 shows the lift coefficient values calculated from the unfiltered data, the data acquired using a hardware 30 Hz low-pass filter, and the same data with a moving average smoothing applied. The unfiltered lift signal contains high-frequency electrical noise near 100 Hz and a mechanical vibration between 15 and 20 Hz. This vibration is evident in both the air and water when the motor is run, with and without the wing attached. There is a frequency shift between the air and the water, thus the inertial data acquired in the air are smoothed before they are subtracted from the force data acquired

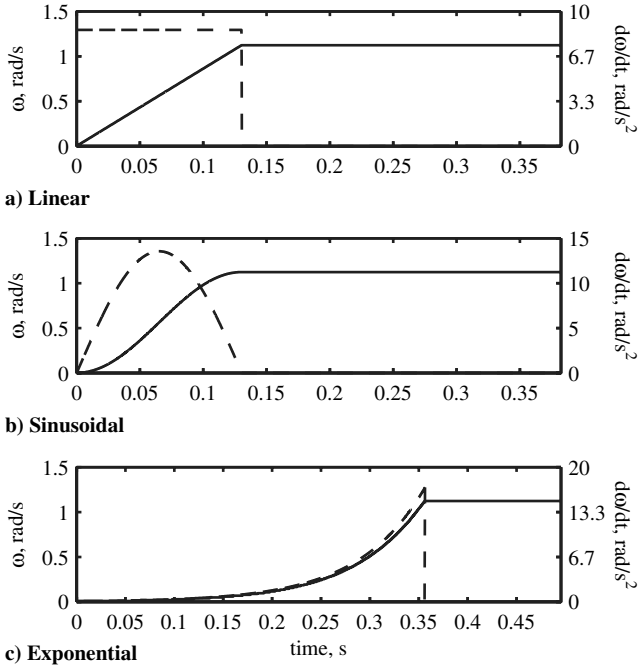

Fig. 3 Commanded wing kinematics for first quarter-stroke accelerating over 0.25 chords: angular velocity (solid) and acceleration (dashed) as a function of time.

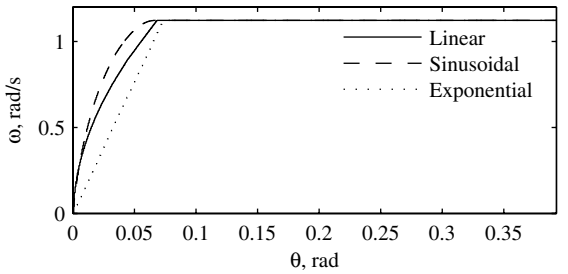

Fig. 4 Commanded wing kinematics for the first quarter-stroke: angular velocity for a wing accelerating over the first 0.25 chords of travel.

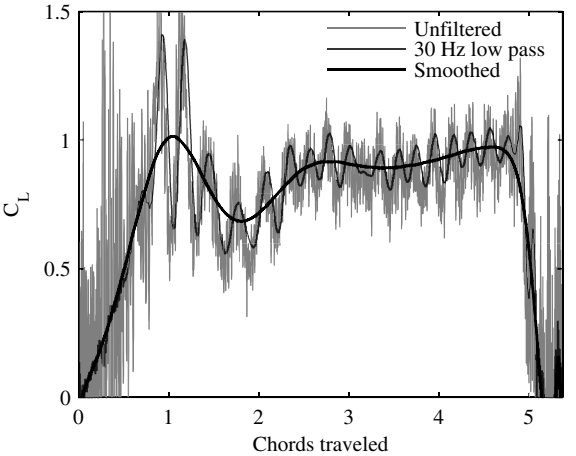

Fig. 5 Lift coefficient for the exponential velocity profile accelerating in 0.60 chords.

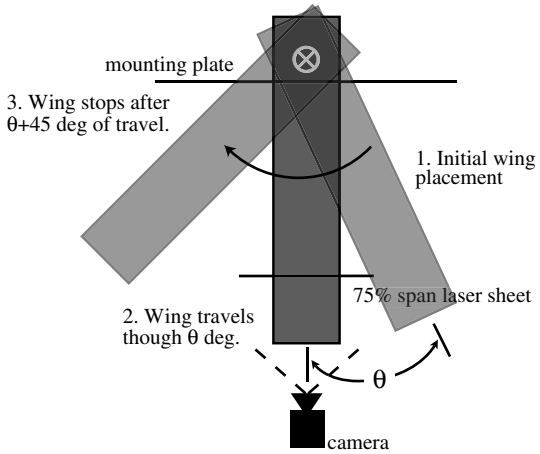

Fig. 6 Chordwise PIV setup.

in the water. The force data shown in the following plots were acquired with the low-pass filter in place to remove the electrical noise; the inertial data was subtracted and the result smoothed to eliminate the vibrations from the signal.

D. Particle Image Velocimetry

PIV was performed using a LaVision FlowMaster 4S digital PIV with a high-resolution high-speed camera capable of up to 1000 frames per second at a resolution of 1024×1024 pixels and a double-cavity laser.

To obtain PIV data for chordwise slices of the waving wing, the horizontal laser sheet entered the tank through the side wall, and the camera was placed below the tank, as in Fig. 6. Images were taken at one-half, three-quarter, and seven-eighth spans throughout the wing stroke. Each case was repeated between 5 and 50 times. Analysis of the early data demonstrated that a smaller number of averages was sufficient in all cases.

Vestosint 7182 particles with a specific gravity of 1.02 were used to seed the flow, appearing in the images with a diameter of 2 to 3 pixels. Images were taken at frame rates between 50 and 750 Hz at a resolution of 1024×1024 pixels with a 20×20 cm field of view. These frame rates resulted in a 3- to 5-pixel particle displacement within the image pairs. The width of the image is 1.6 chord lengths, or 28 deg of the wing stroke, and particles averaged 3 pixels in diameter. PIV images were processed in two passes, with interrogation windows decreasing from 32×32 to 16×16 pixels, with Gaussian weighting and a 50% overlap. The average velocity field was obtained by averaging the velocity components at each spatial point. The final data have a resolution of seven vectors per centimeter, or 88 vectors across the chord.

The flow development over the waving wing is expected to depend on the time history of the motion and not the physical orientation in the tank. To minimize errors that may arise when the laser sheet and the camera are at an angle to the air–Perspex–water interface, the laser and the camera were set up parallel and normal to the tank bottom or wall. The wing was then started at different positions

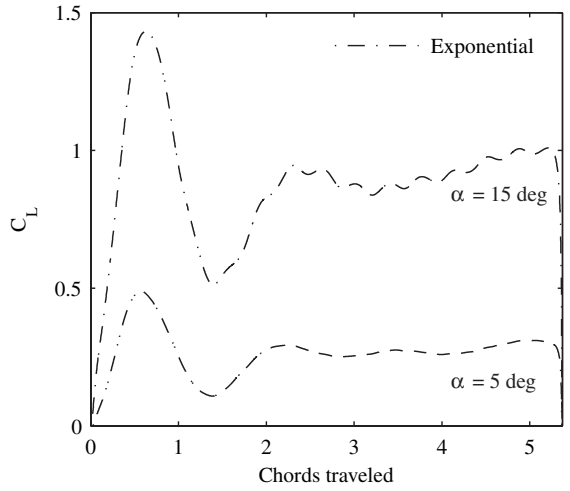

a) Accelerating over 0.10c

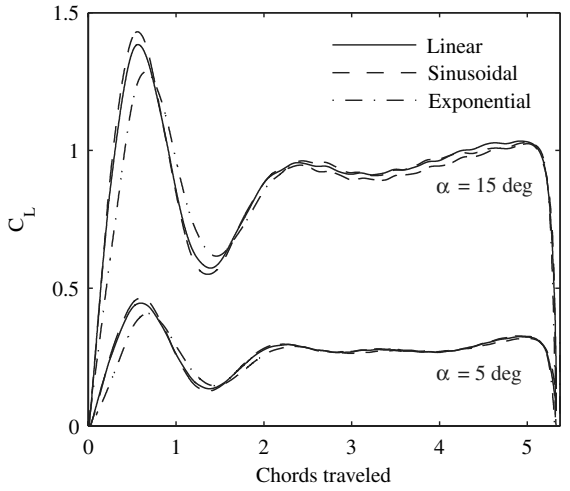

b) Accelerating over 0.25c

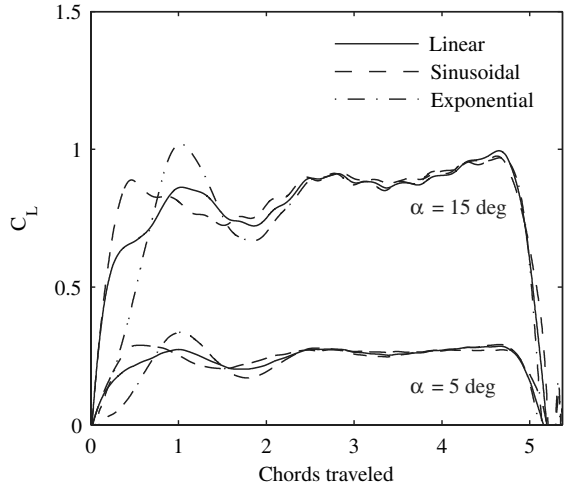

c) Accelerating over 0.60c

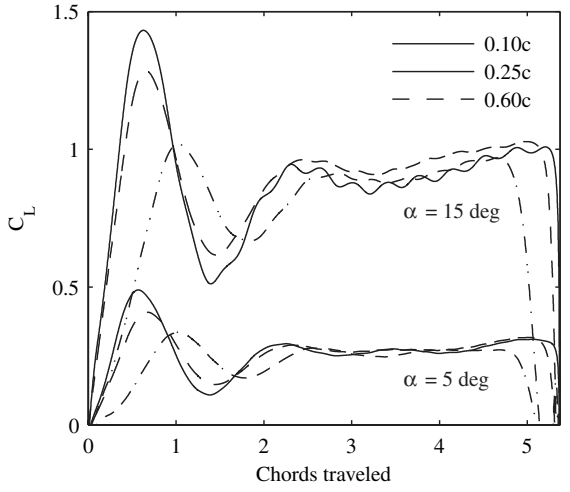

d) Exponential velocity profiles

Fig. 7 Lift coefficients for waving wing.

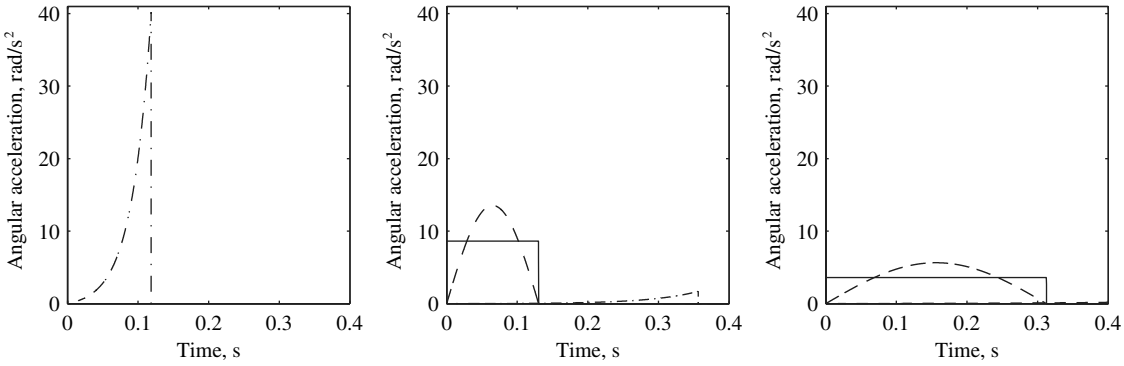

Fig. 8 Angular acceleration for the three velocity profiles: linear (solid line), sinusoidal (dashed line), and exponential (dashed–dotted line).

relative to the laser sheet and the camera. Regardless of the starting position, the wing continued waving 45 deg past the vertical to allow the flow to continue developing while the data were recorded. For travel past 45 deg, the laser sheet and the camera were tilted to remain normal to the wing.

In the highly separated, unsteady flow that develops over the waving wing, it is useful to identify the vortices present in order to track their development and shedding. The vortex identification algorithm, as suggested by Graftieaux et al., was applied to the velocity field [28]. A scalar function λ at point P is defined as

$$\lambda(P) = \frac{1}{N}\sum_{S} \sin(\theta_M)$$

where S is a two-dimensional area centered on point P, N is the number of points inside S, and M is a point that lies on S. The angle between the radius vector from P to M and the relative velocity at point M is θ_M. The relative velocity at point M is the total velocity at that point minus the average velocity across the area S. When P is at the center of an axisymmetric vortex and is a measure of the vortex strength, λ is at its maximum [28].

E. Experimental Uncertainty

The wing angle of attack is accurate to within 1/60th of a degree, and the position is accurate to within 0.2 deg or 0.06 mm at a three-quarter span. The error on the force coefficients is ± 0.03, with an rms of 0.30 in C_L and 0.75 in C_D at $\alpha = 15$ deg. The total error for the PIV measurements, $\epsilon_{\text{tot}} = \epsilon_{\text{bias}} + \epsilon_{\text{rms}}$, was first estimated using the trends and values reported in the literature. For the current PIV setup, $\epsilon_{\text{bias}} \approx -0.01$ due to the loss of pixels [29]. The random error can be expressed as the sum of the uncertainty due to a particle image diameter of 3 pixels, displacement between 1 and 3 pixels, and density averaging of eight particles per window:

$$\epsilon_{\text{rms}} = 0.009 + 0.01 + 0.025 = \pm 0.04$$

The total error becomes $\epsilon_{\text{tot}} = +0.03/-0.05$ pixels. The error was also estimated by evaluating PIV images with a known displacement. An artificial image was generated with an average of 15 3-pixel particles per 16×16 interrogation widow. This image was displaced by 1, 2, 3, or 4 pixels and evaluated with the LaVision DaVis 7.2 software. The rms error for these images with constant displacement was ± 0.01 pixels. To account for the error due to imperfect particle image shapes, intensities, and image noise, real images of the waving wing were artificially displaced and evaluated. The rms error for these images was 0.03 pixels, or 1.7% of the displacement. This value agrees well with the value estimated from the literature.

III. Results and Discussion

A. Force Data

Figure 7 shows the averaged and smoothed lift coefficients for a waving wing at a 5 and 15 deg angle of attack, accelerating to maximum velocity in 0.10, 0.25 and 0.60 chords. It can be seen that changing the angle of attack primarily changes the magnitude of the measured force, whereas the shape of the curve remains much the same. All of the curves are characterized by an initial steep increase in the lift coefficient, leading to a lift peak followed by a sharp drop and subsequent recovery to an intermediate level that is then maintained for the rest of the constant velocity portion of the wing stroke. It appears that after two to three chord lengths of travel (at a three-quarter span, corresponding to a 34 to 51 deg of rotation) the lift nears a steady-state value. The shape of the lift curve shown here, including the initial lift peak, is very similar to those reported by Dickinson and Götz at $Re < 1,000$ [17].

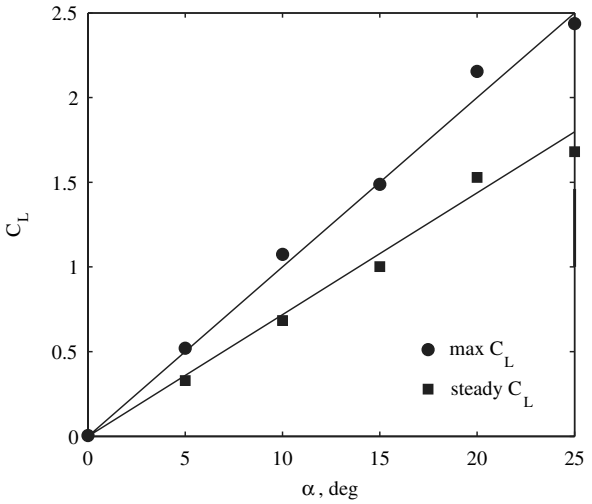

Fig. 9 Lift coefficient as a function of angle of attack.

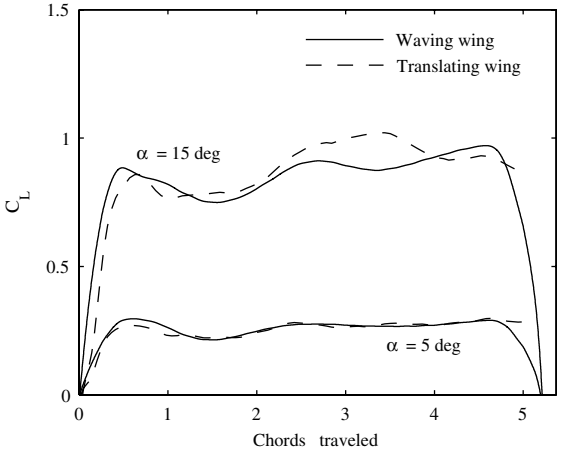

Fig. 10 Comparison of unsteady lift coefficients observed for waving and translating wings accelerating over 0.60 chords.

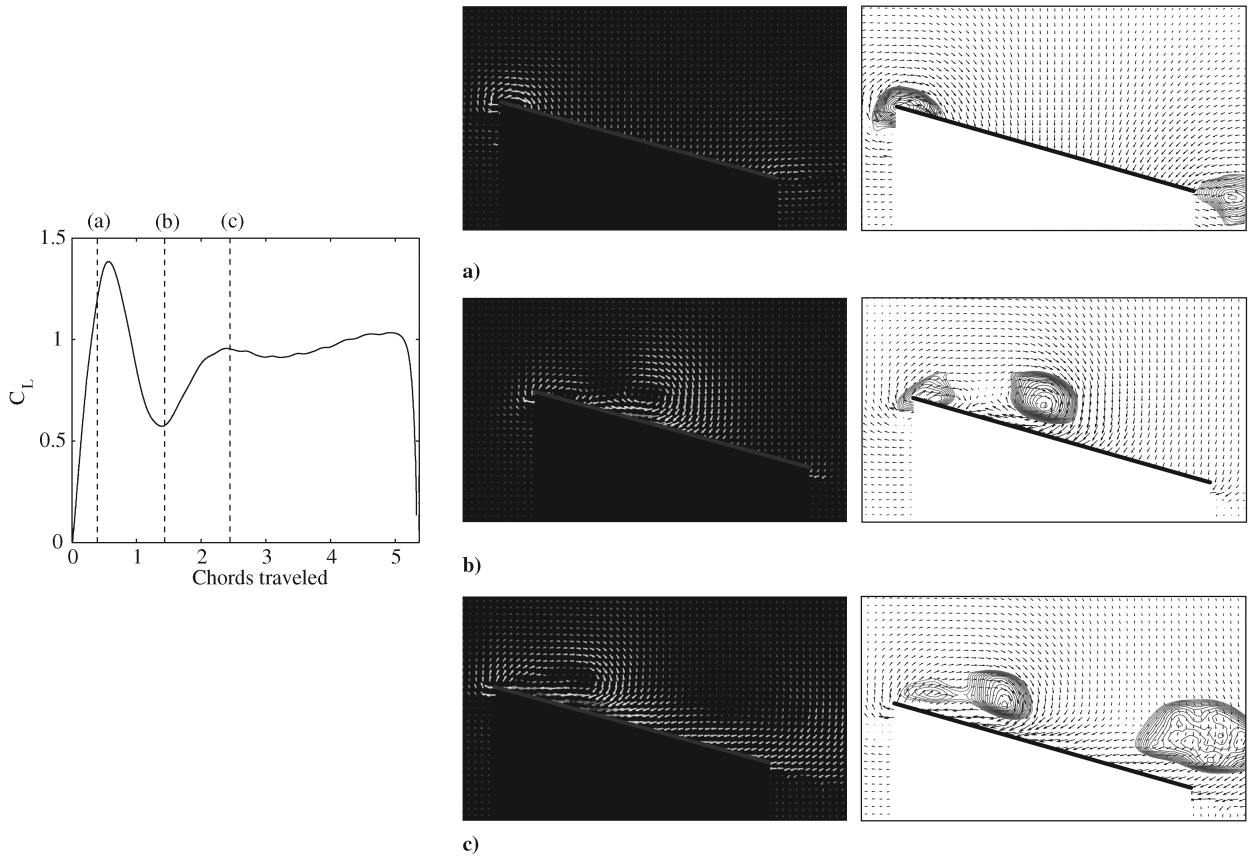

Fig. 11 Flowfield observed at three points during the wing stroke: point a, near the initial lift peak at $x/c = 0.45$ c; point b, at the lift minimum at $x/c = 1.50$ c; and point c, at the onset of the quasi-steady period $x/c = 2.39$ c. Force history (left), velocity field (center), and contours of λ (right) for a waving wing with constant acceleration over 0.25 chords.

The main differences due to different acceleration patterns (shown in Fig. 8) are observed in the early stages of the wing stroke. The slowest acceleration profile is the exponential over 0.60 chords, not even visible in Fig. 8c, with the next slowest being the constant acceleration. Both of these velocity profiles result in a relatively low delayed lift peak past one chord of travel, as in Fig. 7c. Maximum lift coefficients for the linear, sinusoidal, and exponential velocity profiles accelerating in 0.60 c are 0.87, 0.88 and 1.01.

At higher accelerations, the effect of acceleration on the lift peak diminishes, and all of the curves show a pronounced maximum of approximately 50% above the steady-state value near 0.60 chord lengths traveled, well into the constant velocity portion of the wing stroke. The largest acceleration studied is the exponential over 0.10 chords, with a maximum of 40.2 rad s^{-1} and a maximum lift coefficient of 1.42. Over 0.25 chords, the maximum acceleration is 8.6, 13.6, and 1.6 rad s^{-1} for the linear, sinusoidal, and exponential velocity profiles with maximum lift coefficients of 1.34, 1.39, and 1.26, as in Fig. 7b. Despite the large difference in the acceleration, the lift peaks in Figs. 7a and 7b are of similar magnitude and timing. It is interesting to note that the timing of the transient lift peak does not change significantly, whether the wing is accelerated over 0.10 or 0.25 chords, suggesting that the sharp lift peak evident in the force data is due to aerodynamic effects rather than inertia.

Lift curves at a 5 deg angle of attack look much like those at 15 deg with a lower $C_{L_{max}}$ and steady-state value. C_L levels off near 0.95 for $\alpha = 15$ deg or 0.27 for $\alpha = 5$ deg after 2.5 chords of travel for all wing kinematics. For any profile accelerating in 0.10 or 0.25 chords, the maximum C_L occurs near 0.6 chords of travel. C_L versus α for the waving wing (constant acceleration over 0.25 chords) at an angle of attack from 0 to 25 deg is given in Fig. 9. Here, max C_L is the maximum C_L achieved at the lift peak, as shown in Fig. 7. The steady C_L refers to the mean value measured between three and four chords of travel, where the lift levels out. Both lift coefficients appear to be linear in α. The line of best fit for the maximum lift coefficient is $1.82\pi\alpha$, and it is $1.31\pi\alpha$ for the quasi-steady lift coefficient.

Beckwith and Babinsky performed experiments on an impulsively started flat-plate wing towed in pure translation through a water tank [19]. Figure 10 shows the unsteady lift coefficients measured on the waving wing as compared with their sliding wing. Only the constant acceleration over 0.60 chords is shown here, as faster accelerations are not available for the sliding wing. The force history for the two cases is very similar. Lift curves at the higher angle of attack resemble those at Reynolds numbers of less than 1000 reported by Dickinson and Götz [17].

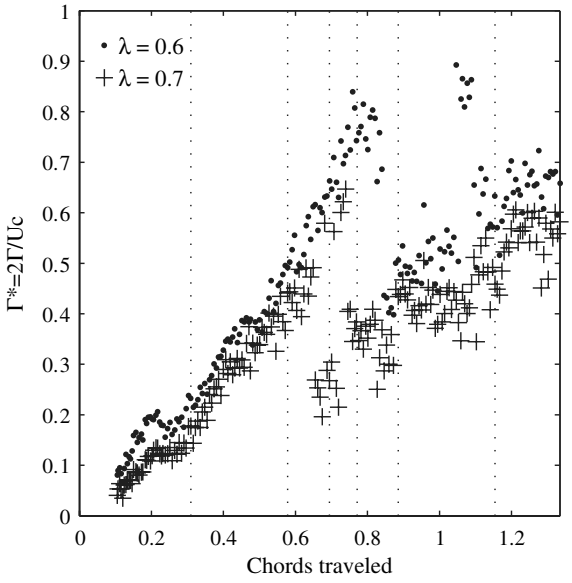

Fig. 12 Normalized circulation computed from PIV data.

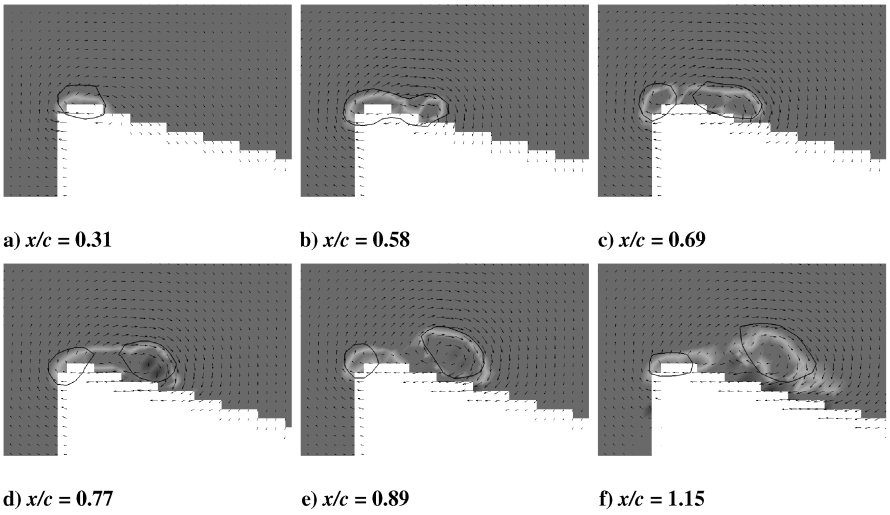

Fig. 13 Circulation of the first LEV with vorticity field and $\lambda = 0.7$ contour.

B. Flowfield

Taking a closer look at the flow during the early stages of motion, Fig. 11 compares both the velocity field and the λ contours to the force history at three points in time for the waving wing undergoing constant acceleration over 0.25 chord lengths of travel at a three-quarter span. There are noticeable differences in the flow pattern at these points in time. First, at point a, a distinct LEV forms on the suction side of the plate. The starting vortex is visible just downstream of the trailing edge. At the minimum lift point b, this vortex has shed and moved downstream while a new LEV forms. As the lift approaches the steady-state value at point c, several vortices coexist above the wing. After this time, there is a continuous pattern of shedding vortices in a quasi-periodic fashion. Unlike previous studies at much lower Reynolds numbers, there is no evidence of an attached LEV over an extended period of time. The images in Fig. 11 suggest that the rapid buildup of lift during the initial stages of the wing stroke is due to the development of the attached LEV and the movement of the starting vortex away from the wing.

C. Leading-Edge Vortex Circulation

Again considering a constant acceleration over 0.25 chords, the circulation of the LEV was computed by integrating along a contour of λ to find the circulation:

$$\Gamma = \int u \cdot \mathrm{d}s$$

The computed circulation was then normalized by the local free-stream velocity and the wing chord. Figure 12 shows the normalized circulation of the first LEV formed at a half-span and at a 15 deg angle of attack. Each data point on the chart was computed from a separate snapshot of the velocity field, as measured using PIV. Figure 13 shows the $\lambda = 0.7$ contour on top of the velocity and vorticity fields for the points marked on the previous figure.

From the start of the wing stroke, an attached LEV begins to form, and almost all of the vorticity in the flowfield is contained within the $\lambda = 0.7$ contour. The circulation of this LEV grows steadily until the point of maximum lift at $x/c = 0.58$. From Fig. 12, the maximum strength of the attached LEV is near $\Gamma^* = 0.45$, at which point the LEV has elongated and a second region of high vorticity has appeared within the $\lambda = 0.7$ contour (Fig. 13b). As the wing continues to move, the downstream portion of the LEV sheds, and the two regions of vorticity become separate vortex cores, as shown in Fig. 13c. Here, the first LEV has been shed and is moving downstream. A second LEV remains attached to the wing and is growing.

Near $x/c = 0.69$, it is difficult to reliably track the first vortex, and Γ^* values jump between 0.25 and 0.60. Most of the vorticity is still contained within the λ contours, but there is also vorticity moving between the two vortices. As the wing stroke continues, the separated LEV continues to move downstream and entrain this vorticity. Eventually, this vortex rolls up at into a more coherent structure at $x/c = 0.89$, and the Γ^* values become more reliable. The first vortex continues to move downstream and away from the still-attached second LEV. Vorticity is still present between the two vortex cores, and the first vortex continues to entrain some of this vorticity, causing the vortex to strengthen slightly. This accounts for the small upward trend in Γ^* past $x/c = 1.0$.

Although the trends are the same, it can be seen in Fig. 12 that the exact circulation value is sensitive to which λ contour the integration is performed over. Although the first LEV is developing, circulation

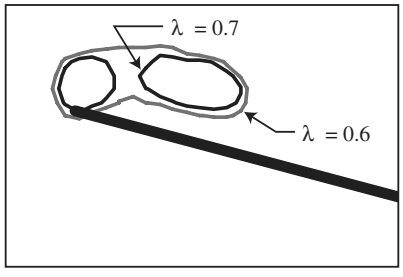

Fig. 14 Velocity field and $\lambda = 0.6, 0.7$ contours for $x/c = 0.69$.

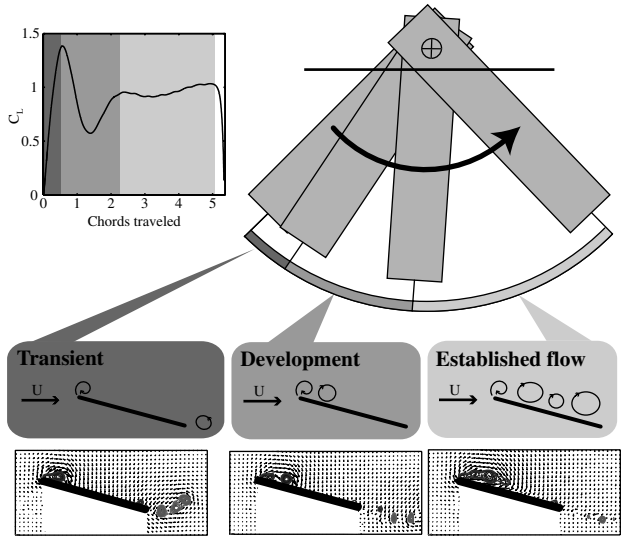

Fig. 15 The three stages of flow development on an impulsively started waving wing: transient, development, and established flow.

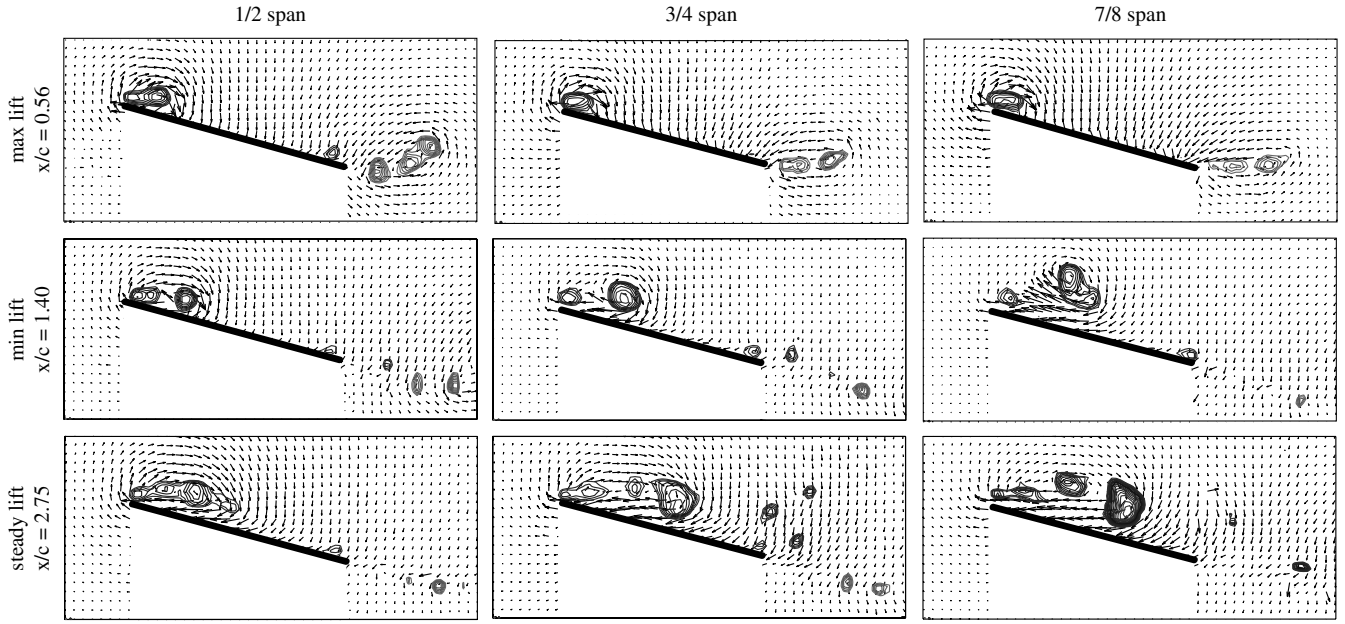

Fig. 16 The λ distribution measured at three spanwise cross sections.

values are similar along both the $\lambda = 0.6$ and 0.7 contours, because the two contours lie very close together. When the first vortex sheds, there is some difficulty identifying the two separate vortices reliably. Larger λ contours are closer to the vortex core, so integrating around a 0.7 contour may result in an underestimation of vortex strength if the vortex core is larger than that contour, but integration around a lower level contour makes it more difficult to identify individual vortices. Figure 14 shows the 0.7 and 0.6 contours for $x/c = 0.69$. At this point in time, the 0.7 contour clearly identifies two vortices (Fig. 13c), but the two vortices are close enough together that the 0.6 contour encompasses them both. Integrating around the 0.6 contour results in an overestimate of the vortex strength (Fig. 12). Once the two vortices have moved further apart (past $x/c = 0.89$), the two sets of λ contours once again lie nearly on top of each other, and the resulting Γ^* values are consistent.

By computing the circulation of the LEV it has been found that the initial vortex grows quickly until the point of maximum lift, $x/c = 0.58$. Just past this point the first LEV is shed and a second leading edge begins to form. The first vortex, now moving downstream, continues to grow slowly by entraining vorticity located between the two vortices. As the two vortices move further apart the first vortex rolls up into a more coherent structure and continues to pass over the wing.

D. Flow Development Model

Based on these observations, it is proposed that the flow on an impulsively started waving wing develops over three stages, as illustrated in Fig. 15. At the start of the wing stroke, during the initial transient, the flowfield is characterized by the growth of a strong LEV. Flow separates at the sharp leading edge and quickly forms a LEV, which remains attached to the wing. During this phase, the strengthening of the LEV causes a rapid increase in lift. This phase ends when the vortex sheds from the leading edge. The ultimate strength of the LEV and its development are influenced by the wing's acceleration pattern. Slower accelerations produce a slower vortex growth and reduce the strength at separation. However, above a certain level of acceleration, the vortex development becomes independent from the kinematics.

The next flow observed on the waving wing is the developing flow, beginning with the separation of the initial LEV. Flow continues to separate over the leading edge, and a second LEV forms. Because the first vortex is no longer close to the wing surface, its effect on lift is diminished, and the new LEV does not achieve the same ultimate strength before it sheds. In this phase, the total lift is relatively low.

Finally, in the established flow phase, a periodic pattern of vortex shedding from the leading edge is observed. During this phase, there are typically three to four vortices present above the wing at all times, producing a relatively high lift coefficient. At this point, the structure of the flowfield appears to settle into a periodic vortex shedding, but it is not yet certain how many chord lengths must be traveled before the flow is truly in a periodic quasi-steady state.

E. Three-Dimensional Effects

Figure 16 shows three cross sections of the λ distribution for absolute values greater than 0.6 measured at three spanwise locations on the wing. The flow is similar in all spanwise locations, suggesting that three-dimensional effects are small. All vortices appear to be of similar size and at a comparable stage of their development. There is, however, some indication that the vortex on the outer sections (7/8 span) detaches from the surface somewhat earlier. This could be a result of the outer wing having traveled further in nondimensional terms (i.e., chord lengths) or an effect of the interaction with the tip flow. Further studies will focus on this aspect of the three-dimensionality of the flow, including the effect of spanwise flow along the velocity gradient and the interaction between the LEVs and the tip vortex.

IV. Conclusions

Experiments have been performed on flat-plate wings in unsteady rotation at $Re = 60,000$ with a focus on the development of lift during the early part of the wing stroke. The rotating wing experiment is a fully three-dimensional simplification of the flapping-wing motion observed in nature. The spanwise velocity gradient and the stopping and starting acceleration preserve key features of the wing stroke that are neglected by other experimental setups. High-speed PIV has been used to capture the unsteady velocity field around the waving wing, and force data have been acquired for several sets of wing kinematics.

All of the flows investigated showed similar behavior, and three-dimensional effects were found to be small. High lift (approximately 1.5 times the quasi-steady value) is achieved during the first chord length of travel, due to the presence of a strong attached LEV. After the initial LEV separates, lift values drop as it passes downstream over the wing, and a second LEV forms. LEVs continue to form, grow, and separate, but subsequent vortices are not as strong as the first one, and the lift values level out. Because the translational phase of the typical insect wing stroke is between two and four chord lengths of travel, the initial lift transient and subsequent flow

development phases on a waving wing are likely to be significant for lift production on a flapping-wing vehicle. Wing kinematics had only a small effect on the aerodynamic forces produced by the rotating wing. Quasi-steady lift and drag forces were very similar for all acceleration patterns tested. In the early stages of the wing stroke, the velocity profile affected both the timing and the magnitude of the lift peak for low accelerations. However, at high accelerations, the velocity profile ceased to be significant. The circulation of the LEV has been measured and agrees well with force data, thus supporting the proposed model of flow development.

Acknowledgments

The authors gratefully acknowledge financial support provided by the Air Force Research Laboratory European Office of Aerospace Research and Development grant FA 8655-07-1-3082 and the National Science Foundation.

References

[1] Ellington, C. P., "Insects Versus Birds: The Great Divide," 44th AIAA Aerospace Sciences Meeting and Exhibit, AIAA Paper 2006-35, Jan. 2006.

[2] Ellington, C. P., "The Aerodynamics of Hovering Insect Flight, 6: Lift and Power Requirements," *Philosophical Transactions of the Royal Society of London, Series B: Biological Sciences*, Vol. 305, No. 1122, Feb. 1984, pp. 145–181. doi:10.1098/rstb.1984.0054

[3] Altshuler, D. L., Dudley, R., and Ellington, C. P., "Aerodynamic Forces of Revolving Hummingbird Wings and Wing Models," *Journal of Zoology*, Vol. 264, No. 04, Dec. 2004, pp. 327–332. doi:10.1017/S0952836904005813

[4] Jones, A. R., Bakhtian, N. M., and Babinsky, H., "Low Reynolds Number Aerodynamics of Leading-Edge Flaps," *Journal of Aircraft*, Vol. 45, No. 1, Jan.–Feb. 2008, pp. 342–345. doi:10.2514/1.33001

[5] Azuma, A., *The Biokinetics of Flying and Swimming*, Springer–Verlag, Tokyo, 1992.

[6] Gad-el Hak, M., "Control of Low-Speed Airfoil Aerodynamics," *AIAA Journal*, Vol. 28, No. 9, Sept. 1990, pp. 1537–1552. doi:10.2514/3.25250

[7] Hertel, H., *Structure–Form–Movement*, Reinhold, New York, 1963.

[8] Ellington, C. P., "The Aerodynamics of Hovering Insect Flight, 3: Kinematics," *Philosophical Transactions of the Royal Society of London, Series B: Biological Sciences*, Vol. 305, No. 1122, Feb. 1984, pp. 41–78. doi:10.1098/rstb.1984.0051

[9] Dudley, R., *The Biomechanics of Insect Flight*, Princeton Univ. Press, Princeton, NJ, 2000.

[10] Ellington, C. P., van den Berg, C., Willmott, A. P., and Thomas, A. L. R., "Leading-Edge Vortices in Insect Flight," *Nature*, Vol. 384, No. 6610, Dec. 1996, pp. 626–630. doi:10.1038/384626a0

[11] van den Berg, C., and Ellington, C. P., "The Vortex Wake of a "Hovering" Model Hawkmoth," *Philosophical Transactions of the Royal Society of London, Series B: Biological Sciences*, Vol. 352, No. 1351, 1997, pp. 317–328. doi:10.1098/rstb.1997.0023

[12] van den Berg, C., and Ellington, C. P., "The Three-Dimensional Leading-Edge Vortex of a "Hovering" Model Hawkmoth," *Philosophical Transactions of the Royal Society of London, Series B: Biological Sciences*, Vol. 352, No. 1351, 1997, pp. 329–340. doi:10.1098/rstb.1997.0024

[13] Birch, J. M., and Dickinson, M. H., "Spanwise Flow and the Attachment of the Leading-Edge Vortex on Insect Wings," *Nature*, Vol. 412, No. 6848, Aug. 2001, pp. 729–733. doi:10.1038/35089071

[14] Birch, J. M., Dickson, W. B., and Dickinson, M. H., "Force Production and Flow Structure of the Leading Edge Vortex on Flapping Wings at High and Low Reynolds Numbers," *Journal of Experimental Biology*, Vol. 207, No. 7, 2004, pp. 1063–1072. doi:10.1242/jeb.00848

[15] Tarascio, M. J., Ramasamy, M., Chopra, I., and Leishman, J. G., "Flow Visualization of Micro Air Vehicle Scaled Insect-Based Flapping Wings," *Journal of Aircraft*, Vol. 42, No. 2, March–April 2005, pp. 385–390. doi:10.2514/1.6055

[16] Ramasamy, M., and Leishman, J. G., "Phase-Locked Particle Image Velocimetry Measurements of a Flapping Wing," *Journal of Aircraft*, Vol. 43, No. 6, Nov.–Dec. 2006, pp. 1867–1875. doi:10.2514/1.21347

[17] Dickinson, M. H., and Götz, K. G., "Unsteady Aerodynamic Performance of Model Wings at Low Reynolds Numbers," *Journal of Experimental Biology*, Vol. 174, No. 1, Jan. 1993, pp. 45–64.

[18] Ringuette, M. J., Milano, M., and Gharib, M., "Role of the Tip Vortex in the Force Generation of Low-Aspect-Ratio Normal Flat Plates," *Journal of Fluid Mechanics*, Vol. 581, No. 1, June 2007, pp. 453–468. doi:10.1017/S0022112007005976

[19] Beckwith, R., and Babinsky, H., "Impulsively Started Flat Plate Wing," *Journal of Aircraft*, Vol. 46, No. 6, Nov.–Dec. 2009, pp. 2186–2189. doi:10.2514/1.46382

[20] Wilkins, P. C., and Knowles, K., "The Leading-Edge Vortex and Aerodynamics of Insect-Based Flapping-Wing Micro Air Vehicles," *Aeronautical Journal*, Vol. 113, No. 1142, April 2009, pp. 253–262.

[21] Okamoto, M., and Azuma, A., "Experimental Study on Aerodynamic Characteristics of Unsteady Wings at Low Reynolds Numbers," *AIAA Journal*, Vol. 43, No. 12, Dec. 2005, pp. 2526–2536. doi:10.2514/1.14813

[22] Ol, M., "Vortical Structures in High Frequency Pitch and Plunge at Low Reynolds Number," 37th AIAA Fluid Dynamics Conference and Exhibit, Vol. AIAA Paper 2007-4233, June 2007.

[23] Radespiel, R., Windte, J., and Scholz, U., "Numerical and Experimental Flow Analysis of Moving Airfoils with Laminar Separation Bubbles," 44th AIAA Aerospace Sciences Meeting and Exhibit, AIAA Paper 2006-501, Jan. 2006.

[24] Usherwood, J. R. and Ellington, C. P., "The Aerodynamics of Revolving Wings: 1. Model Hawkmoth Wings," *Journal of Experimental Biology*, Vol. 205, No. 11, 2002, pp. 1547–1564.

[25] Usherwood, J. R., and Ellington, C. P., "The Aerodynamics of Revolving Wings, 2: Propeller Force Coefficients from Mayfly to Quail," *Journal of Experimental Biology*, Vol. 205, No. 11, 2002, pp. 1565–1576.

[26] Nolan, G. R., "Aerodynamics of Vortex Lift in Insect Flight," Ph. D. Thesis, Univ. of Cambridge, Cambridge, England, U.K., Sept. 2004.

[27] Ellington, C. P., "The Aerodynamics of Hovering Insect Flight, 4: Aerodynamic Mechanisms," *Philosophical Transactions of the Royal Society of London, Series B: Biological Sciences*, Vol. 305, No. 1122, Feb. 1984, pp. 79–113. doi:10.1098/rstb.1984.0052

[28] Graftieaux, L., Michard, M., and Grosjean, N., "Combining PIV, POD and Vortex Identication Algorithms for the Study of Unsteady Turbulent Swirling Flows," *Measurement Science and Technology*, Vol. 12, No. 9, Aug. 2001, pp. 1422–1429. doi:10.1088/0957-0233/12/9/307

[29] Raffel, M., Willert, C. E., and Kompenhans, J., *Particle Image Velocimetry: A Practical Guide*, Springer, New York, 1998.